Journal of Materials Research and Technology 41 (2026) 1883–1897

Contents lists available at ScienceDirect

Journal of Materials Research and Technology

journal homepage: www.elsevier.com/locate/jmrt

On the feasibility of electroforming Fe-Co alloys for biodegradable tiny medical devices

Carlos Henrique Michelin Beraldo [a], Carlo Paternoster [a], Francesco Copes [a], Ibrahim Bilem [b], Laurence Dion-Albert [b], Helton José Wiggers [c], Paolo Mengucci [d], Diego Mantovani [a,*]

[a] Laboratory for Biomaterials and Bioengineering (LBB-UL), Canada Research Chair Tier I, Department of Min-Met-Materials Engineering, and CHU de Québec Research Center, Division Regenerative Medicine, Laval University, Quebec, QC, G1V 0A6, Canada
[b] Saguaro Biosciences, La Centrale – Espace Entrepreneurial, Laval University, Quebec, QC, G1V 0A6, Canada
[c] Laboratory for Biomaterials and Bioengineering (LBB-BPK), Associação de Ensino, Pesquisa e Extensão, BIOPARK, Toledo, 85919-899, Brazil
[d] Department SIMAU & UdR INSTM, Università Politecnica Delle Marche, Via Brecce Bianche 12, 60131, Ancona, Italy

ARTICLE INFO

Keywords:
Biodegradable metals
Fe-based alloys
Fe-Co
Electroforming
Degradation

ABSTRACT

Biodegradable metallic alloys made of magnesium, iron and zinc constitute today a recognized alternative to corrosion-resistant alloys, especially for clinical application where temporary support is required. Pure Fe presents interesting mechanical properties, but also a low degradation rate. For this reason, the addition of alloying elements could be effective to improve the corrosion rate of Fe-based alloys. In this work, electroformed Co-containing Fe-based alloys were produced, and their properties investigated. Optical microscopy and X-ray diffraction were used to assess the microstructure, while scanning electron microscopy, atomic force microscopy and contact profilometry were used for the evaluation of the surface topography. Chemical composition was assessed through energy dispersive spectrometry. Potentiodynamic polarization and electrochemical impedance spectroscopy tests assessed the corrosion behavior of the materials. Results showed a complex influence of Co on surface topography and degradation properties of the samples. The electroformed alloys showed an α-Fe microstructure, while the addition of Co led to the modification of some microstructural parameters. Fe-Co alloys also showed a decrease in wettability compared to pure Fe; this was attributed to the formation of a passive layer. For most of the samples, Co addition resulted in superior corrosion resistance. Nevertheless, for sample Fe-5.0Co, a synergy between an unstable passive layer and high nano-scale rugosity (27.6 nm) resulted in increase in the corrosion rate from 0.17 $mm \cdot y^{-1}$ (for pure Fe) to 0.29 $mm \cdot y^{-1}$. Finally, cell viability showed a unique concentration-dependent cytotoxicity of the Fe-Co alloys for fibroblasts, and all samples presented a direct kill mechanism for *E. coli*.

1. Introduction

Bioabsorbable metals have been attracting wide attention from biomedical researchers and medical device engineers, especially regarding their degradation features justifying their use as temporary support medical devices. Their advantage, when compared to the properties of "corrosion-resistant" alloys (AISI316L, CoCr-based alloys, Ti-based, etc.) is that they can be completely degrade, their ions absorbed and finally eliminated through physiological pathways; the functionality of the device must however be guaranteed until the full recovery of the damaged tissue. Their biological performances (*in vitro*, *in vivo* and clinically), and the one of the corrosion products, which may serve also as metabolites to the organism, has been investigated and confirmed [1,2]. Pure iron, zinc and magnesium, as well as their alloys, have been investigated – and magnesium and its alloys has led to implants and devices in clinics [3]. In general, biodegradable metals require to modulate corrosion resistance. For example, Mg-based alloys usually present a high degradation rate, poor ductility and the risk to produce hydrogen [3–5], while Zn-based alloys often show an acceptable degradation rate (between Mg and Fe), but poor mechanical properties and brittleness are still limiting factors [2,6,7].

Recently, increasing attention has been given to iron and its alloys. Despite their high mechanical resistance and ductility, and regardless of their general cytocompatibility, studies have shown that the *in vivo*

* Corresponding author.
E-mail address: diego.mantovani@gmn.ulaval.ca (D. Mantovani).

https://doi.org/10.1016/j.jmrt.2026.01.020
Received 23 July 2025; Received in revised form 5 December 2025; Accepted 4 January 2026
Available online 10 January 2026

Table 1
Bath composition and deposition parameters used in the electroforming process.

Sample	Bath		Deposition	
	Chemical	Concentration ($g{\cdot}L^{-1}$)	Parameter	Condition
e-Fe	$FeCl_2{\cdot}4H_2O$	400	j ($A{\cdot}dm^{-2}$)	2
	$CaCl_2$	80	Time (h)	2
	Sodium saccharine	1.0	Temperature (°C)	90
	0.25			
	Na^+ dodecyl sulfate		pH	1.0
			Stirring	No
Fe-*x*Co	$FeCl_2{\cdot}4H_2O$	227	j ($A{\cdot}dm^{-2}$)	2
	$CoCl_2{\cdot}6H_2O$	x	Time (h)	2
	Boric acid	24.7	Temperature (°C)	90
	Ascorbic acid	8.8	pH	1.0
			Stirring	No

corrosion rate (CR) of iron is rather lower than the *in vitro* one [8–10], and in any case too low for this class of biomedical applications, making essential its improvement to envisage their use as resorbable metals in temporary devices. Alloying iron with other elements constitutes a recognized alternative to increase its degradability [11,12]. Huang, Zheng and Han [13] implanted Zn into pure Fe and observed a roughly three-fold CR increase in Hanks' solution, from 0.027 mm y^{-1} to 0.093 $mm{\cdot}y^{-1}$. The authors attributed the inferior corrosion resistance to the lower standard potential of Zn together with the high distortion energy caused by the implantation, and to the galvanic coupling between Zn- and Fe-rich phases. Huang, Cheng and Zheng [14] produced Fe-Pd and Fe-Pt composites from spark plasma sintering and evaluated the electrochemical properties in Hanks' solution. The results showed a j_{corr} increase compared to pure Fe (0.871 $\mu A{\cdot}cm^{-2}$), that is 1.550 $\mu A{\cdot}cm^{-2}$ for Fe-Pd and 6.698 $\mu A{\cdot}cm^{-2}$ for Fe-Pt; this was considered as a consequence of microgalvanic corrosion. Kupková *et al.* [15] produced a series of Fe-Cu alloys from powder metallurgy; they verified a j_{corr} increase for increasing amounts of Cu, from 48 $\mu A{\cdot}cm^{-2}$ (pure Fe) to 57 $\mu A{\cdot}cm^{-2}$ (3.2 wt.% Cu) and 100 $\mu A{\cdot}cm^{-2}$ (8.0 wt.% Cu), mainly due to the presence of a nobler phase inducing, even in this case, galvanic corrosion.

Another candidate to be considered is cobalt, a less conventional alloying element in biomedical applications. Despite the controversies in its use in biological media due to a low toxicity limit [16], this metal is essential for life in the human body, composing the biologically needed vitamin B12, helping on the prevention of chronic diseases, impacting the correct functioning of the immune system, and others [17]. Studies point out that the bioaccumulation of cobalt in the organism could be considered low, since its excretion largely occurs *via* intestines and kidneys [18,19]. Cobalt is also well-explored due to its antibacterial activity, an interesting appeal for biomedical applications [20]. For instance, Abass et al. [21] explored the effect of cobalt-nanoparticles against multidrug-resistant pathogens and observed a strong antibacterial effect for the concentration of 100 $\mu g{\cdot}mL^{-1}$. Kiani *et al.* [22] synthetized cobalt-doped ferrite nanoparticles targeting gram-positive and gram-negative pathogens and observed a potent antibacterial activity. Furthermore, cobalt was also explored as doping agent for bioactive glasses, showing promising therapeutic use thanks to its pro-angiogenic effect [23].

For intravascular medical devices, such vascular stents, which require to be so tiny (1 to 2 mm in diameter and less than 100 μm in thickness) but so resistant (to radially support the artery when deployed) to allow its crimping around a balloon, then mounting on a catheter, inserted under X-ray observation in the diseased tissue or organ, and deployed at the delivery site, electroforming might constitute the process of choice [10,24]. In fact, electroforming is a process in which a metal or alloy is fabricated *via* its deposition onto a mandrel using an electrolytic solution containing metal ions and further detached [25]. In fact, electroforming is a bottom-up process, much more adapted to the production of tiny structures and complex shapes than other metallurgical processes such as casting or even additive manufacturing processes [24,26]. Finally, from an electrochemical point of view, cobalt is also an interesting alloying element, since it presents close standard electrode potential in comparison to iron (−0.28 V_{SHE} and −0.44 V_{SHE}, respectively). Altogether, one can expect that the co-deposition of these metals using the electroforming process would be facilitated. Nevertheless, although cobalt appears to be a promising alloying element to iron from both biocompatibility and electrochemical perspectives, studies on electroformed Fe-Co alloys for biomedical applications remain scarce in the literature.

The aim of the study was to report on the properties of electroformed Fe-Co alloys for potential biomedical device applications. Four different cobalt concentrations were investigated, between 8 and 23 wt% Co. Specimens were investigated by optical microscopy (OM), and scanning electron microscopy (SEM) coupled with an energy-dispersive X-ray spectrometer (EDS), electron probe microanalysis (EPMA), contact profilometry, atomic force microscopy (AFM), water contact angle (WCA) and X-ray diffraction (XRD). The corrosion behavior of the alloys was evaluated by potentiodynamic polarization (PDP) and electrochemical impedance spectroscopy (EIS). Cell viability and antibacterial activity were also assessed. Finally, AI technology was used to study the cell death mechanism induced by the degradation products of the alloys.

2. Materials and methods

2.1. Chemicals

For the electroforming process, the following reagents were used: iron(II) chloride tetrahydrate 98 % (Thermo Scientific), cobalt(II) chloride hexahydrate 99.9 % (Alfa Aesar), boric acid 99.8 % (Fischer), ascorbic acid 99.8 % (Fischer), calcium chloride 96 % (Fisher), saccharine sodium salt 99 % (Alfa Aesar) and sodium dodecyl sulfate 98 % (Acros). A modified Hanks' balanced salt solution (MHBSS) was used as medium for all the electrochemical analyses; its composition is described in Table S1 (Supplementary Materials) and was based in a previous study [27]. The pH of the solution was adjusted between 7.35 and 7.45 using whether NaOH or HCl 1.0 $mol{\cdot}L^{-1}$. All chemicals were used as received.

2.2. Electroforming process

Electroformed samples were produced in constant current density using a BioLogic SP-300 potentiostat. For this, previously mechanically polished 4.4 cm^2 square substrates of cp-Ti were used as working electrode (cathode), a graphite rod as counter-electrode, and a wire of pure silver as reference electrode. The composition of the electrolytic baths, as well as the parameters of the deposition process, are described in Table 1. After deposition, the samples were manually detached from the working electrode, rinsed with running water, and consecutively with methanol and stocked into a desiccator until further use.

Conditions were named according to the amount of $CoCl_2{\cdot}6H_2O$ salt in the electrolytic bath with the following labels: Fe-1.0Co (1.0 $g{\cdot}L^{-1}$), Fe-2.5Co (2.5 $g{\cdot}L^{-1}$), Fe-5.0Co (5.0 $g{\cdot}L^{-1}$) and Fe-10Co (10 $g{\cdot}L^{-1}$). A condition composed only of electroformed Fe (e-Fe) had no cobalt in the composition and was considered as the reference material in the analysis. The composition of the Fe-Co solutions differed from that used for e-Fe because the addition of cobalt salts altered the deposition mechanism compared to pure iron, requiring modifications to obtain optimized alloy deposition.

Table 2
List of compounds used for phenotype characterization.

Phenotype	Compound	Dose
Apoptosis [30]	Staurosporine	500 nM
Ferroptosis [31]	Erastin	500 nM
Necrosis [32]	Hydrogen peroxyde (H_2O_2)	200 μM
ER stress [33]	Thapsigargin	200 nM
Autophagy [34]	Rapamycin	100 nM

Table 3
Excitation and emission wavelengths for ChromaLIVE™ imaging.

Channel	Excitation wavelength	Emission wavelength
ChromaLIVE-488_Yellow	488 nm	550–630 nm
ChromaLIVE-488_Red	488 nm	630–750 nm
ChromaLIVE-561	561 nm	575–630 nm

2.3. Characterization

The microstructure of the surface and cross-section of the samples were evaluated by means of OM using a Nikon microscope model Epiphot. The samples were cold mounted in acrylic resin, then polished until a mirror surface was obtained. Afterwards, etching was performed by immersing the polished specimen in a 2 % Nital solution for ~15 s and rinsing it in running tap water. SEM surface micrographs were taken with a FEI Quanta 250 electron microscope, using a tungsten filament with a tension voltage of 10 kV. For EDS analysis, an $U_{bias} = 12.5$ kV tension was used. For both SEM and EDS analysis, at least three randomly selected regions of each sample were evaluated. The iron, cobalt and oxygen distributions of the investigated conditions were evaluated by means of EPMA of the cross-sections, using a CAMECA SX-100 electron probe micro-analyzer, with an acceleration voltage of 15 kV and a probe current of 20 nA.

The topography and roughness values of the samples were evaluated using a Bruker Dektak XT contact profilometer. A force F = 0.5 mg was applied to the 5-μm-radius stylus tip of the profilometer, on areas of 1000 μm × 1000 μm; the measurement was carried out five times, on several randomly selected areas for each sample condition. AFM analyses were conducted in a Veeco Dimension TM3100 platform, used in tapping mode and operated with an etched silicon tip (radius <10 nm). The roughness values of R_a and R_q were measured both for 50 μm × 50 μm and 1 μm × 1 μm areas randomly selected in the sample. The wettability of the surface was assessed through a sessile drop water contact angle system, using an AST goniometer model VCA Optima; drop of approximately 1 μL of distilled water was used. The measurement was conducted five times for each sample. XRD was performed using a Bruker D8 Advance diffractometer (Bregg-Brentano geometry) equipped with a Cu tube ($Cu_{K\alpha}$ λ = 1.54056 Å), a graphite monochromator, and operating at V = 40 kV and I = 40 mA, in the angular range 20°–80°. Pattern analysis was performed by the DIFFRAC.EVA software package, and peak indexing was carried out by the search/match facility using the PDF 2 database of the International Center for Diffraction Data (ICDD).

The samples were electrochemically analyzed by the techniques of PDP and EIS to evaluate corrosion behavior, using an Ametek VersaSTAT potentiostat model 3. The system was composed of a saturated calomel electrode (SCE) as reference electrode, a graphite rod as counter-electrode, and the samples as working electrode. All the measurements were conducted in MHBSS at room temperature (T = 25 ± 1 °C), on four specimens for each condition. Open circuit potential (OCP) was carried out during 30 min, and then EIS was performed between 10 kHz and 10 mHz, with an amplitude of ±10 mV *versus* OCP. The fitting process was conducted with the aid of NOVA software. OCP curves can be found in Fig. S1 of the Supplementary Materials. PDP analyses took place right after the EIS measurement, with a scanning rate of 0.5 $mV{\cdot}s^{-1}$, at ± 500 mV *versus* OCP. The corrosion current density (j_{corr}) was obtained using the Tafel method, and the corrosion rate (CR) using Equation (1) [28]:

$$CR = \frac{3.72 \times 10^{-3} \times j_{corr} \times EW}{\rho} \quad \text{Eq. (1)}$$

Where EW (equivalent weight in $g{\cdot}eq^{-1}$) and ρ (material density in $g{\cdot}cm^{-3}$) values differ between each sample due to their composition, and were theoretically calculated using Equations (2) and (3):

$$EW = \frac{1}{\frac{n_{Fe}f_{Fe}}{W_{Fe}} + \frac{n_{Co}f_{Co}}{W_{Co}}} \quad \text{Eq. (2)}$$

$$\rho = f_{Fe}\rho_{Fe} + f_{Co}\rho_{Co} \quad \text{Eq. (3)}$$

Where n is the valence, W the atomic weight (amu) and f the mass fraction of the alloy's elements. Only iron and cobalt were taken into consideration in the calculation.

The indirect cytotoxicity test was performed following the ISO 10993-5:2009 procedure [29]. Before the test, all samples had been sterilized by UV irradiation. Briefly, each side of the samples underwent two 15-min cycles of UV irradiation (254 nm). After that, samples were stored in a sterile 24 multi-well plate until use. Human dermal fibroblasts (HDFs) were used in the following experiments. HDFs were cultured in Dulbecco's modified Eagle's medium (D-MEM) with 10 % fetal bovine serum (FBS), penicillin (100 U/mL) and streptomycin (100 U/mL). Cells were maintained at 37 °C in a saturated atmosphere at 5 % CO_2. Media was changed every two days until a 90 %–95 % confluence was reached. At this point, cells were detached from the plate using trypsin and then re-plated at a ratio of 1:5 used for the experiments. Cells at passage five have been used for the presented tests. For the test, 1 cm^2 samples were immersed in 660 μL of D-MEM culture medium, supplemented with 1 % penicillin-streptomycin for 1 day. After the incubation, the medium has been collected from the samples and subsequently used for the viability tests. These ones have been performed using different concentrations of the extracted media: respectively 100 %, 10 % and 1 % dilutions. Before putting them in contact with cells, extracted media have been supplemented with 10 % fetal bovine serum (FBS). For the 10 % and 1 % dilutions, extracted media were diluted with complete D-MEM medium. One day prior to contact with the extract, HDFs were seeded in the well of a 96 multi-well plate at a density of 20000 cells/cm^2 and incubated at 37 °C and 5 % CO_2 for 24 h in 100 μL/well of complete D-MEM. Cell cultivated in complete D-MEM medium were used as a control (CTRL Plast). The day after, the medium was removed and 100 μL of the 100 %, 10 % and 1 % extracts dilutions were added to the well containing cells and incubated for 24 h. The extracts were then removed and 100 μL of 1 % solution of resazurin sodium salt in complete D-MEM medium were added to the cells and incubated for 4 h at 37 °C and 5 % CO_2. After the incubation, the solutions containing the now reduced resorufin product were collected and fluorescence intensity at a 545 nm_{ex}/590 nm_{em} wavelength was measured with a SpectraMax i3x Multi-Mode Plate Reader. Fluorescence intensity is proportional to cell viability. Statistical significance has been calculated using ANOVA non-parametric Kruskal-Wallis method with Dunn post-test through the software InStat™. Values of $p < 0.05$ or less have been considered significant.

For the Live-Cell Painting assay, HDFs were grown on culture flasks in DMEM medium containing 10 % FBS. Prior to the test, cells were seeded in the wells of 96 multi-well plate at a density of 20000 cell/cm^2 (3 wells per condition). After 24 h of incubation, the medium was replaced by growth containing 0.1 % ChromaLIVE™ dye (1:1000 dilution). ChromaLIVE™ is a non-toxic multichromatic dye with three excitation/emission wavelength pairs. Cells were than put back in culture for 24 h. After this incubation period, cells were exposed to different treatments: extracts obtained from the e-Fe condition (e-Fe); extracts obtained from the Fe-5.0Co (Fe-5.0Co). Both extracts were used at a 100

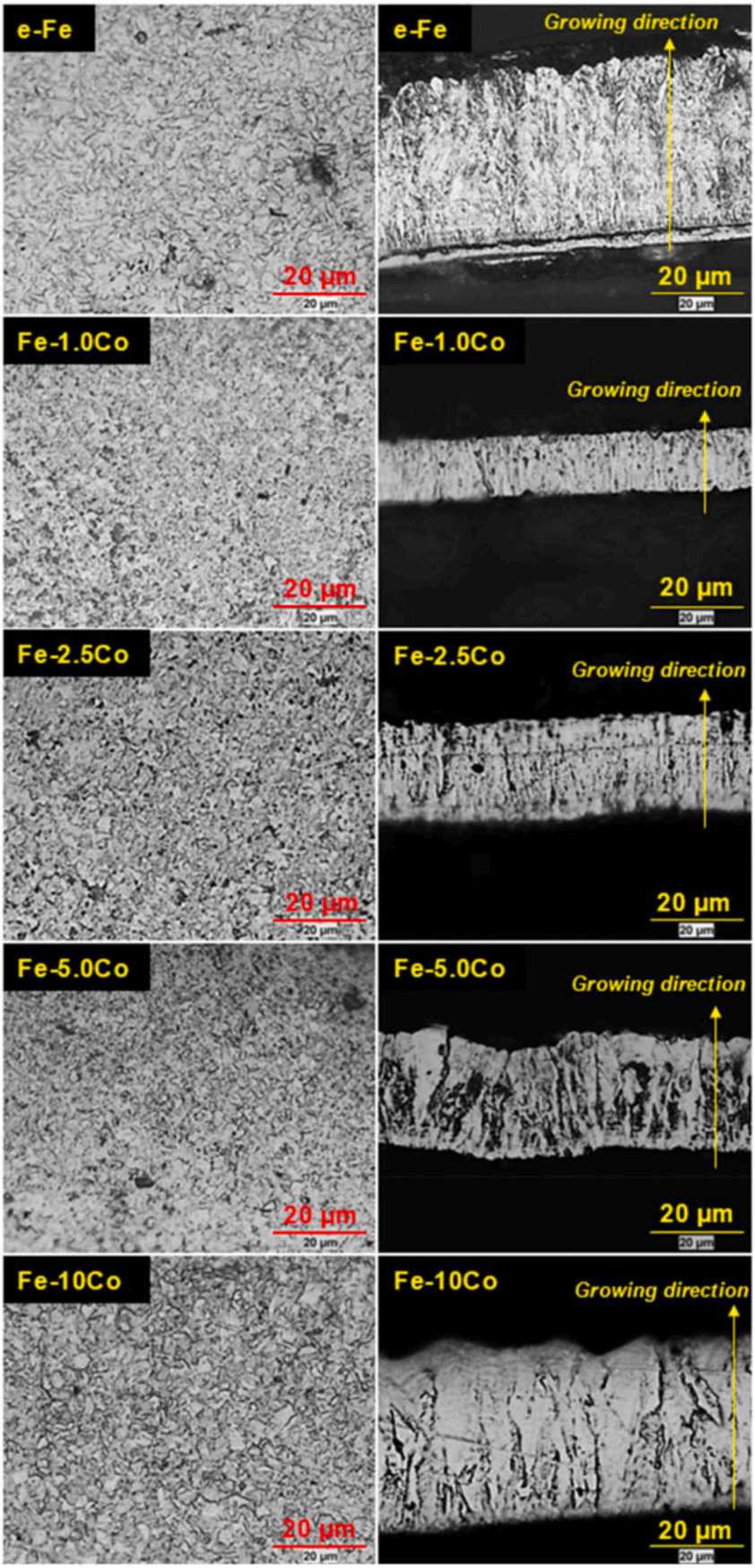

Fig. 1. OM images of the surface (left column) and cross-section (right column) of the samples after etching in 2 % Nital. For all samples, scale bars represent 20 μm.

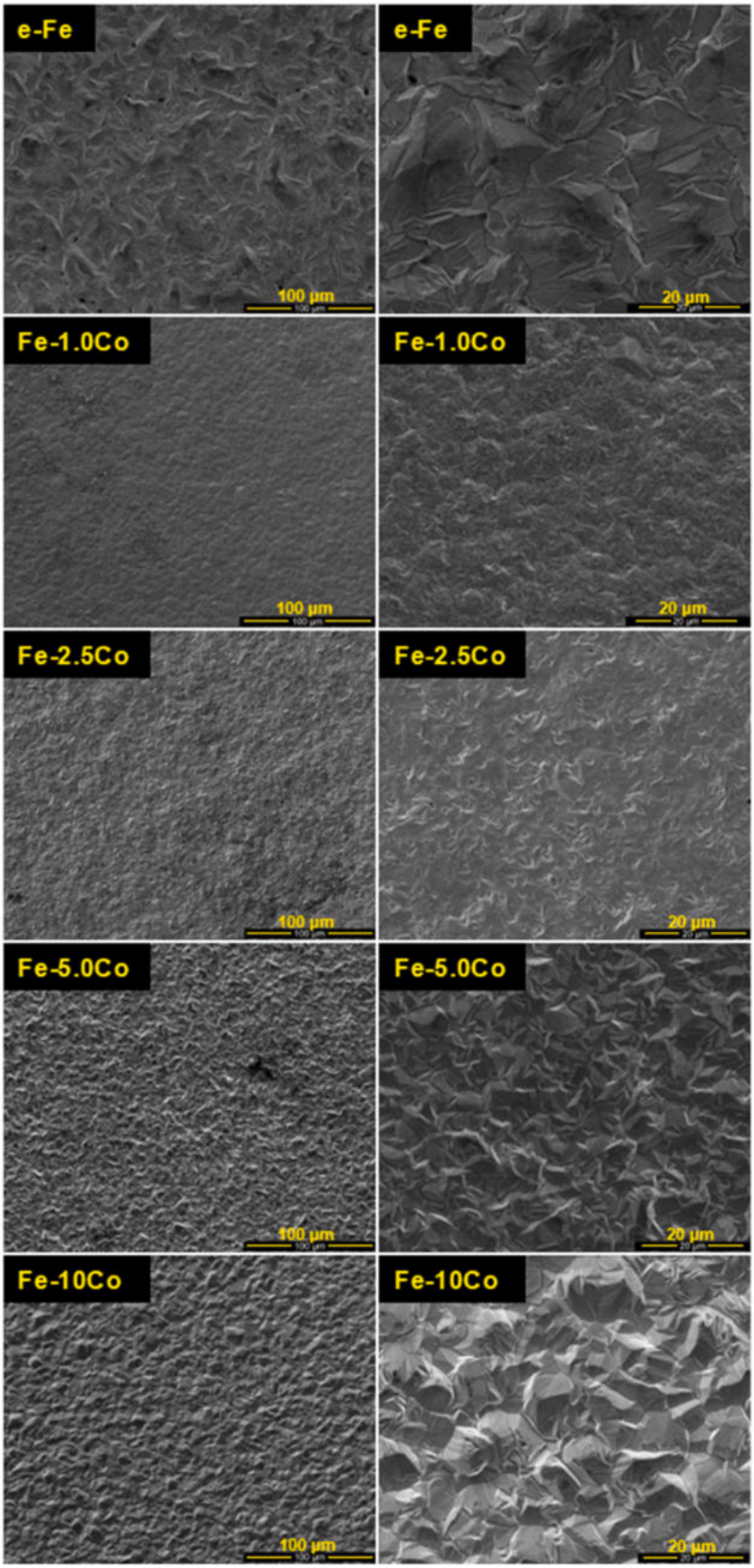

Fig. 2. SEM images of the surface of the samples in different magnifications. Scale bars: 100 µm (first column) and 20 µm (second column).

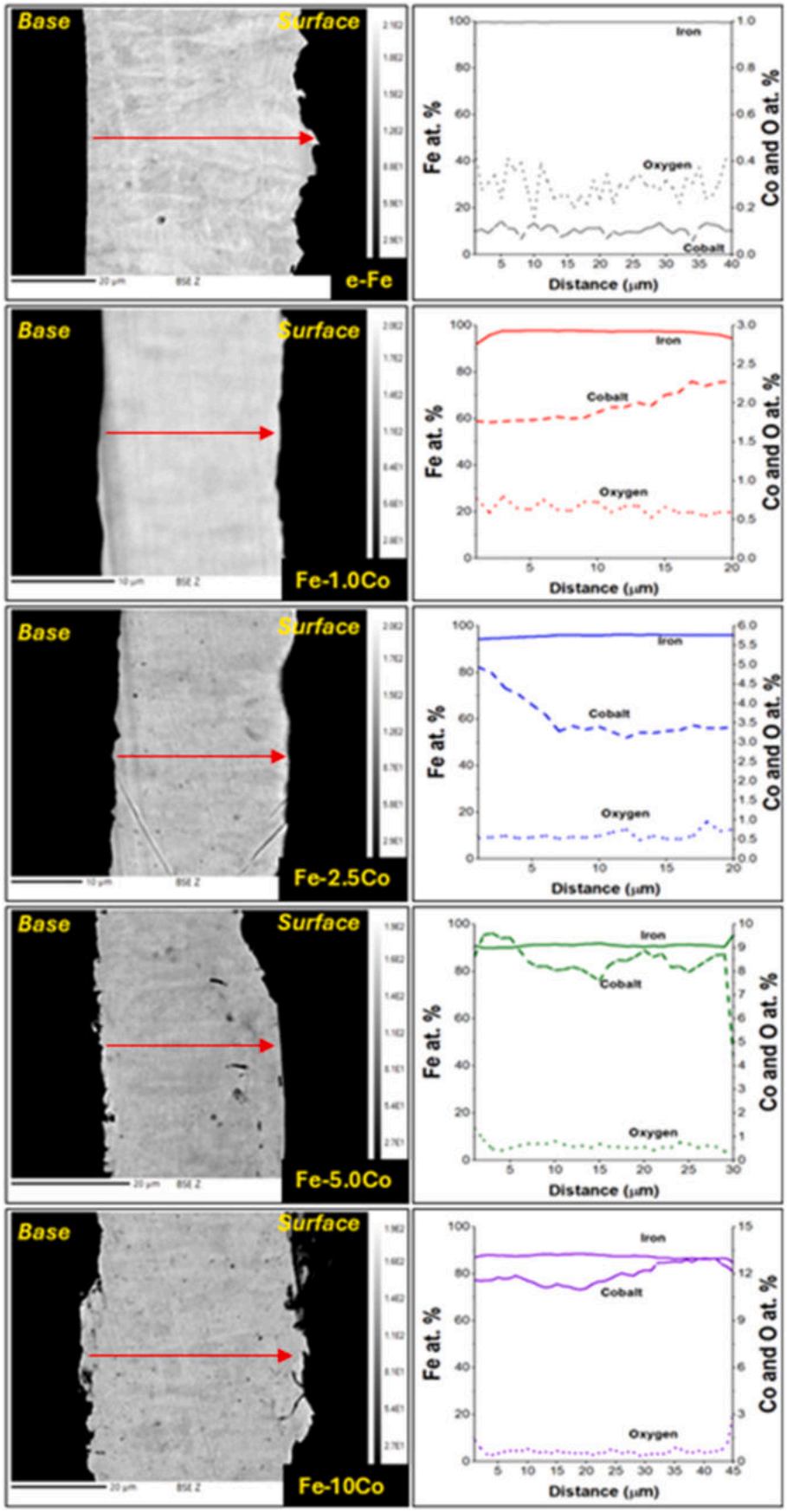

Fig. 3. EPMA line scans for Fe, O and Co in the cross-section of the samples.

Table 4
Roughness and contact angle values of the samples.

Sample	Roughness						WCA (°)
	Profilometry		AFM				
	R_a (μm)	R_q (μm)	R_a (nm)		R_q (nm)		
			50 × 50 μm²	1x1 μm²	50 × 50 μm²	1x1 μm²	
e-Fe	1.9 ± 0.2	2.5 ± 0.4	915.5	20.6	1118.0	27.8	61 ± 4
Fe-1.0Co	0.4 ± 0.1	1.1 ± 0.5	243.2	19.0	303.6	25.0	98 ± 2
Fe-2.5Co	0.7 ± 0.1	1.0 ± 0.1	360.9	16.2	443.4	24.3	101 ± 3
Fe-5.0Co	1.1 ± 0.2	1.5 ± 0.3	414.0	27.6	511.6	31.3	96 ± 3
Fe-10Co	3.9 ± 1.3	4.6 ± 1.7	639.1	19.5	791.6	26.3	103 ± 1

% dilution. In parallel, HDFs were treated with a panel of reference compounds, each known to induce distinct cell phenotypes related to cell death and stress responses. These well-characterized compounds served as mechanistic benchmark, enabling the exploration of potential modes of action through which the tested extracts affect the biological response of HDFs. The compounds and their corresponding working concentrations are listed in Table 2.

Untreated cells culture media were used as a control (CTRL). After 1, 4, 8 and 24 h of incubation the cells were imaged, using ZEISS LSM800 confocal laser scanning microscope, equipped with Zen Blue software (Zeiss, Germany) and a 20X objective. Table 3 provides the imaging settings used to acquire fluorescent images of ChromaLIVE-stained HDFs. Nuclei were counterstained using Hoechst 33342 (100 ng/mL). For each replicate well, four fields of view were captured, resulting in a total of 12 images per condition per time point.

Acquired images of HDFs stained with ChromaLIVE™ were processed using an open-source software CellProfiler for automated image analysis and high-content feature extraction. An analysis pipeline was developed to segment individual cells by identifying both nuclear and cytoplasmic compartments, followed by quantification of single-cell morphological features, including shape, size, texture, granularity and intensity across multiple channels. A total of 817 features were extracted per cell across all treatment conditions. The resulting data were stored in an SQLite database for downstream analysis using CellProfiler Analyst. Subsequently, the extracted features were aggregated at the well level and subjected to dimensionality reduction using t-Distributed Stochastic Neighbor Embedding (t-SNE). Briefly, t-SNE condenses high-dimensional data into a two-dimensional space, where similar data points are placed close together and dissimilar points are positioned farther apart. This enables the visualization of treatment-specific and temporally dynamic clustering patterns based on cell morphological profiles.

For the antibacterial activity test, *Escherichia coli*, *E. coli*, (ATCC 8937) was seeded on fresh sterile Mueller–Hinton agar in Petri dishes and incubated overnight at 37 °C in an inverted position. Then, a single colony was picked and incubated in 20 mL of fresh sterile Mueller–Hinton broth overnight at 37 °C under shaking at 150 rpm. After the bacterial growth, sterile glycerol at 15 % v/v was added for cryoprotection and the bacteria suspension aliquots were frozen at −20 °C. The CFU/mL of the stocks after thawing was determined using the log dilution method. The method used was based on ASTM E2922-23 [35]. *E. coli* was diluted to a concentration of 10^6 CFU/mL in Mueller–Hinton broth (1:500 v/v). Then, square 1 cm^2 samples were incubated in 2 mL of the inoculated medium. The samples were incubated 24 h at 37 °C and 150 rpm. After this period, the inoculated medium was transferred to a sterile centrifuge tube (Eppendorf). Serial dilutions (10x) were performed from inoculated bacteria that were in contact with the samples, following a logarithmic scale. 100 μL of bacteria with 900 μL of diluted medium. 100 μL of each dilution was plated on Muller Hinton agar in 90 mm petri dishes. The plates were incubated in an inverted position at 37 °C overnight. The positive control was the inoculum in a sterile tube without any antibacterial compound. The number of colonies was counted and recorded in colony-forming units per milliliter (CFU/mL). The experiments were performed in triplicate, and the results are expressed as the average in logarithmic scale (log CFU/mL) and standard deviation.

3. Results and discussion

Fig. 1 shows the microstructure of the surface and cross-section of all samples after etching in 2 % Nital. It was spotted a predominant presence of one single phase, expected to be ferrite (α-Fe), based on the Fe-Co equilibrium diagram [36]. From the surface of the Fe-Co alloys, no significant differences were noticed in terms of microstructure, but sample Fe-10Co appeared to exhibit somewhat coarser grains relative to the other samples. At low quantities, cobalt is described to cause grain refinement, which was already observed in ductile iron [37] and tin-based alloy [38] containing <1 % Co. However, at high cobalt concentration, coarser grains could be related to the crystallinity of the alloy. Anjum *et al.* [39] observed that the addition of cobalt in iron oxide nanoparticles resulted in materials with higher crystallinity. In addition, Rozlin and Alfantazi [40] observed that increasing the amount of iron in Co-Fe alloys was responsible for the refinement of the structure.

Regarding the cross-section of the samples, all samples presented a columnar morphology, typical of electrodeposited samples, and it is a result of a growth competition between adjacent grains [41]. No remarkable differences were evidenced between the microstructures of the sample Fe-1.0Co, Fe-2.5Co and Fe-5.0Co, but for sample Fe-10Co, coarser grains could be checked in comparison to the other ones.

SEM results of the surface of all samples are presented in Fig. 2. The morphology of surface in the e-Fe sample was very similar to that obtained by Mostavan *et al.* [42], composed of homogeneously distributed faceted peaks with similar sizes. Such morphology is related to the nucleation and coalescence of the crystallites, that strongly depends on the bath composition and deposition parameters. Remarkable changes in morphology were obtained by the addition of cobalt on the composition of the alloys. For samples containing low cobalt addition, Fe-1.0Co and Fe-2.5Co, smooth surfaces can be seen, as well as a decrease in the dimensions of the surface features observed in the e-Fe. This can be related to the refinement in the microstructure [43] caused by the addition of cobalt, as also suggested in the OM results.

Increasing the cobalt amount to higher values (Fe-5.0Co and Fe-10Co) led to the appearance of well-defined structures on the samples. These structures were like those observed in other Co-containing alloys [44,45]. It is worth pointing out that the surface of the sample Fe-10Co presented more regular-sized features than the sample Fe-5.0Co, which seemed to have the most irregular topography between the Fe-Co alloys. Finally, from the EDS results, the composition found for the samples were: Fe-1.0Co (wt.% Fe: 92 and wt.% Co: 8), Fe-2.5Co (wt.% Fe: 90 and wt.% Co: 10), Fe-5.0Co (wt.% Fe: 83 and wt.% Co: 17) and Fe-10Co (wt.% Fe: 77 and wt.% Co: 23).

From EPMA analysis, shown in Fig. 3, it is possible to observe that the

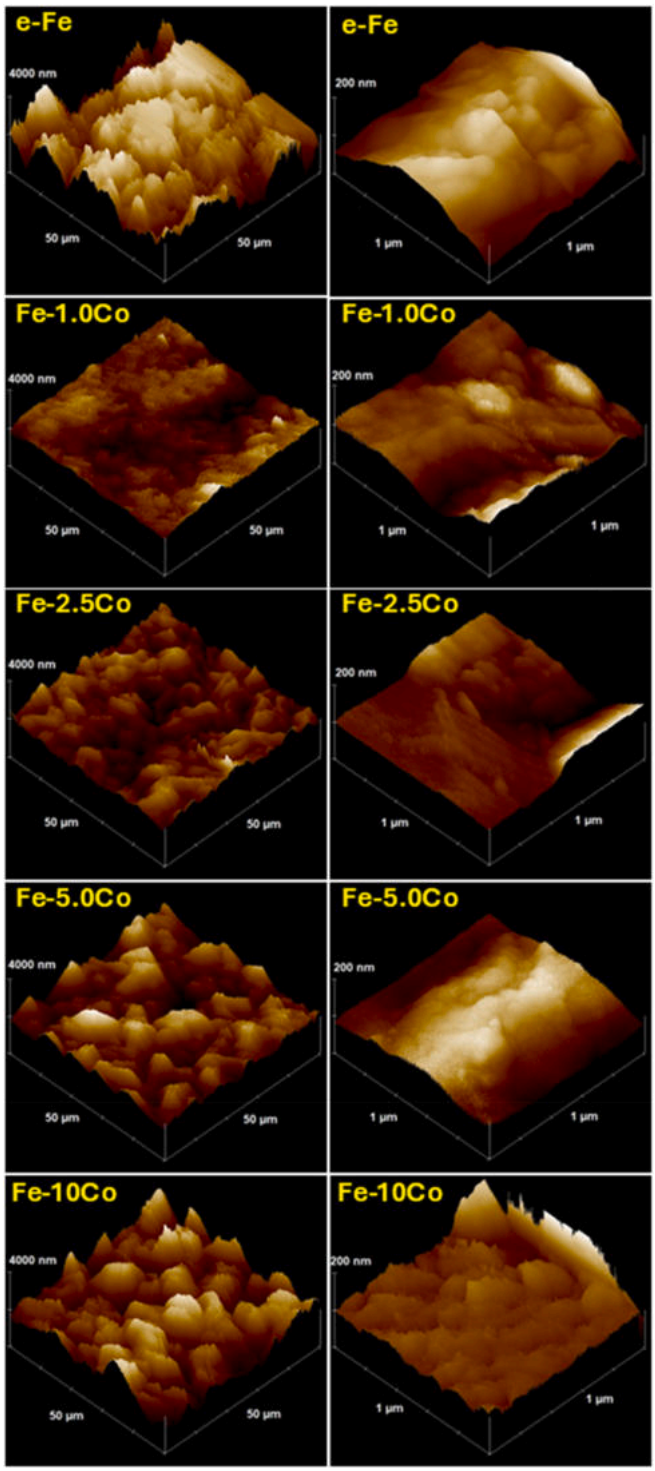

Fig. 4. AFM images of the surface of the samples. Left: 50 µm × 50 µm and right: 1 µm × 1 µm.

distribution of iron and cobalt was mostly homogeneous through the cross-section of the samples. Regarding the oxygen distribution, it remained approximately constant at around 0.5 at.% for all samples, with exception of sample Fe-10Co. In this case, the surface presented around 3 at.% oxygen, which can be related to adsorbed oxygen, or sample oxidation. Finally, a slightly higher concentration of cobalt was generally observed in the base of the samples followed by a slight decrease in its concentration, except in the case of the sample Fe-1.0Co. This might indicate that in the initial steps of the deposition cobalt had a higher tendency to reduce than iron. Such a preferential deposition of cobalt in the initial steps is not necessarily due to its nobler characteristic than iron, but rather a result of a complex mechanism involving molar ratios, deposition preferences and electron depletions near the cathode [46].

In Table 4 the values of roughness and WCA for the different conditions are presented. Samples e-Fe and Fe-10Co presented the highest average roughness, R_a, 1.9 µm and 3.9 µm, respectively. On the hand, the samples Fe-1.0Co and Fe-2.5Co presented the lowest values, 0.4 µm and 0.7 µm, respectively, probably due to grain refinement [47]. These results are compatible with what was observed in SEM and OM tests, where the samples Fe-1.0Co and Fe-2.5Co presented similar morphology and microstructure between them, as well as between the samples e-Fe and Fe-10Co. For sample Fe-5.0Co, it was possible to observe that besides the fact that it presented a lower R_a in the contact profilometry test than samples e-Fe and Fe-10Co, it presented the highest roughness at small scales (1 × 1 µm, obtained by means of AFM), which means that at small scales it presented an irregular topography. From the AFM analyses shown in Fig. 4, it is possible to observe that sample Fe-5.0 Co is the one that showed more pronounced hills (lighter color areas) and valleys (darker areas) among all the samples.

From the WCA results, one can observe that the sample e-Fe presented the lowest value among all the samples, around 62°. For the Fe-Co electroformed alloys, no significative differences in hydrophobicity were observed for the different conditions, but an increase in hydrophobicity was noticed in comparison to the e-Fe sample. This is probably due to the formation of a more hydrophobic layer on the surface of the alloys caused by the addition of cobalt, since the wettability of a solid is the result of the synergy of surface topography and chemical composition [48]. In fact, Bazhan, Ghodsi and Mazloom [49] observed a decrease in wettability in their Co_x-Fe_{3-x}-O_4 thin films with the increasing amount of cobalt, result of a change in the morphology of the material. Changes in the morphology of the Fe-Co alloys were also observed in the present study, as observed in the SEM analysis.

XRD analysis of the samples is presented in Fig. 5. Patterns showed a prevalence of ferrite phase (α-Fe) with a preferential (110) orientation. The results also indicated that an increase of the cobalt amount increased the crystallinity of the sample (see analysis with Rietveld refinement, Fig. S2 in the Supplementary Materials) as well as the intensity of the preferential (110) orientation. This means that as cobalt amount increased, an increased number of (110) planes parallel to the surface was obtained, increasing the reflection for this orientation. For all the conditions, no visible peak related to other phases were observed, possibly due to the low amount of cobalt in the alloys. According to the Fe-Co equilibrium diagram, only α-Fe would be expected for all the investigated conditions. Even if other authors [50,51] report the presence of different microstructures and phases in electrodeposited materials, a metallurgical process that normally occurs out of equilibrium, in the alloys analyzed in the present work, no other phase was found.

Fig. 6 shows representative PDP curves for the electroformed alloys. Table 5 shows the obtained parameters for each curve of the conditions studied in the present work. It was possible to observe that the increase of cobalt in the alloys displaced the E_{corr} towards nobler values, indicating that from a thermodynamic point of view increasing the cobalt content made the alloy more resistant to corrosion. Regarding the anodic branches on the curves, significant differences in the β_a values were not observed, but passivation was found for all the conditions, as a result of the formation of a surface passive layer; this phenomenon was also observed for other iron-based electrodeposited alloys [52–54], and confirmed by the WCA results. Finally, regarding the cathodic branches, a trend towards lower values of β_c for the Fe-Co alloys comparing to the pure iron could be found. This suggested that the addition of cobalt to iron could enhance the hydrogen evolution rate of the system by modifying the electronic state and increasing the presence of active sites on the surface of the alloys [55].

From the j_{corr}, R_p and CR values, different effects were observed by

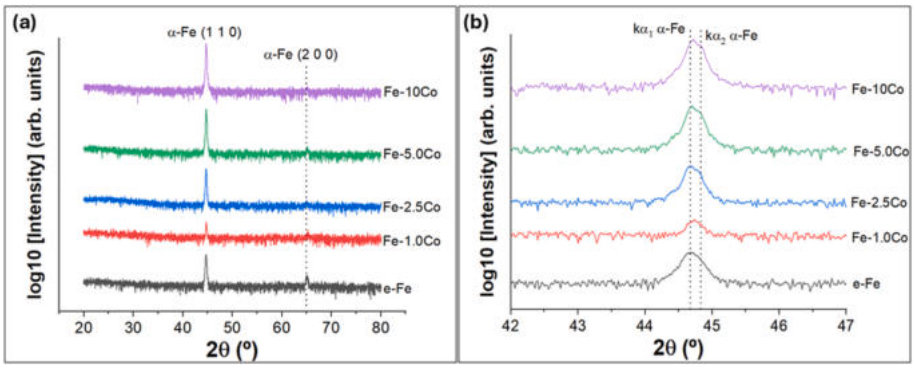

Fig. 5. Representative diffractograms of the samples: (a) all 2θ range and (b) zoomed range in the region of between 42° and 47°.

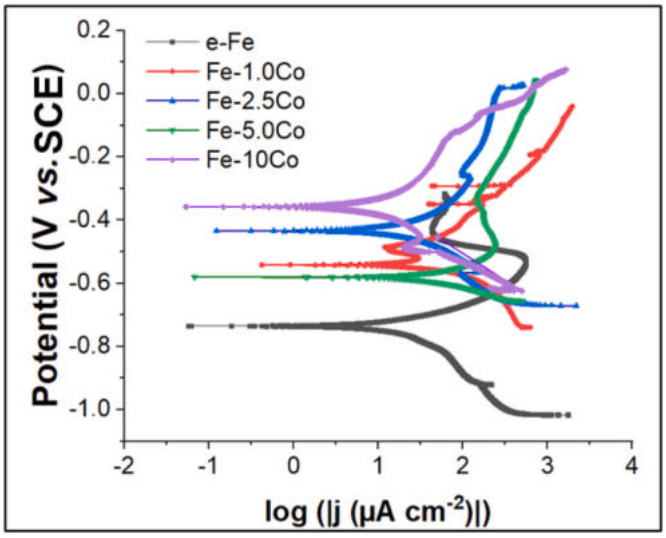

Fig. 6. Representative PDP curves of the studied conditions.

the addition of cobalt. First, the obtained CR for pure iron was 0.17 $mm{\cdot}y^{-1}$. This value was like the one obtained by Moravej *et al.* [10] for cast-thermally-treated (CTT) iron foils ($CR_{CTT\text{-}Fe} = 0.16 \pm 0.04$ $mm{\cdot}y^{-1}$, obtained with MHBSS as electrolyte). This value was considered generally low [56,57] by the authors, based on other works, which pointed out that the *in vivo* CR of CTT pure Fe could be even lower than the *in vitro* one.

For low cobalt additions, such as in Fe-1.0Co conditions, it was not observed a significant CR variation compared to pure iron. CR and j_{corr} tended to decrease with the addition of cobalt, as seen in samples Fe-2.5Co and Fe-10Co. These samples also presented the highest values of R_p, around 2.1 kΩ and 3.7 kΩ, respectively. In fact, the addition of cobalt was reported to improve the corrosion resistance of different alloys, due to the retardance in the anodic reactions and formation of a corrosion-resistant oxide layer [58,59]. In addition, these conditions also showed a more regular topography, as seen from the SEM and profilometry tests. Such a characteristic was well-described in the literature to increase the resistance against corrosion in metals [60–62], and could be one of the reasons for the j_{corr} reduction and CR increase. The increase in crystallinity, as discussed in XRD, could be responsible for superior corrosion resistance. In general, crystalline alloys are expected to present lower corrosion resistance than their amorphous analogues because of the presence of defects, heterogeneity and low reactivity to form corrosion products that can induce an improved corrosion resistance [63]. Nevertheless, the compositions of the alloys play a very important role in this case, which can lead to the formation of a stable passive layer that can increase the corrosion resistance, such as discussed by Berger *et al.* [64] and Guo *et al.* [65].

An out-of-the-trend behavior was observed for sample Fe-5.0Co, which presented the highest CR among all the conditions, that is 0.29 $mm{\cdot}y^{-1}$, as well as a low R_p value, around 0.7 kΩ. This condition presented the highest roughness at nanoscale and the most irregular topography, as discussed in the SEM and AFM tests. This could result in superior geometric area and active sites on the surface, inducing the corrosion occurrence [61,66]. A factor potentially contributing to this behavior could be the change in nucleation mechanisms induced by varying cobalt contents. Sahari *et al.* [67] reported that the electronucleation mechanism of CoFe depositions depends on the Co/Fe ratio, where an instantaneous mechanism was found at 10:1 (nuclei form quickly at available sites before significant growth occurs) and a progressive at 1:1 (nuclei form gradually over time while earlier clusters continue to grow). Such variations in nucleation can lead to grains with different sizes and distributions, resulting in heterogeneous morphologies of the surface. For sample Fe-5.0Co, the composition may correspond to a transitional regime between different nucleation mechanisms.

Complementary to the PDP tests, EIS was performed (Fig. 7). In general, two semi-circles were observed in the Nyquist diagram, indicating two different time-constants. The time-constant at high-middle frequency is related to the interface layer/solution, and the one at low frequency to the interface metal/solution. For Fe-5.0Co and Fe-10Co, the two time-constants presence was clearly visible, indicating that the passive layer formed on the surface of these conditions had a pronounced effect on their corrosion behavior. Additionally, Fe-10Co presented the development of predominant capacitive behavior, as seen in the Bode plot, which indicated the formation of a surface layer that prevented the solution penetration toward the bulk. For samples e-Fe, Fe-1.0Co and Fe-2.5Co, the two time-constants seemed to converge into

Table 5
Data obtained from the potentiodynamic polarization test.

Sample	E_{corr} (mV *vs.* SCE)	j_{corr} ($\mu m{\cdot}cm^{-2}$)	β_c ($mV{\cdot}dec^{-1}$)	$\lvert\beta_a\rvert$ ($mV{\cdot}dec^{-1}$)	R_p (kΩ)	CR ($mm{\cdot}y^{-1}$)
e-Fe	−702 ± 48	14.4 ± 1.6	116 ± 8	69 ± 14	1.30 ± 0.13	0.17 ± 0.02
Fe-1.0Co	−520 ± 95	15.9 ± 0.7	76 ± 8	68 ± 3	0.74 ± 0.05	0.18 ± 0.01
Fe-2.5Co	−438 ± 49	8.2 ± 1.9	81 ± 13	70 ± 8	2.06 ± 0.59	0.09 ± 0.02
Fe-5.0Co	−590 ± 17	25.5 ± 1.4	107 ± 2	66 ± 3	0.69 ± 0.04	0.29 ± 0.02
Fe-10Co	−358 ± 58	5.1 ± 1.4	97 ± 9	74 ± 9	3.7 ± 0.92	0.06 ± 0.02

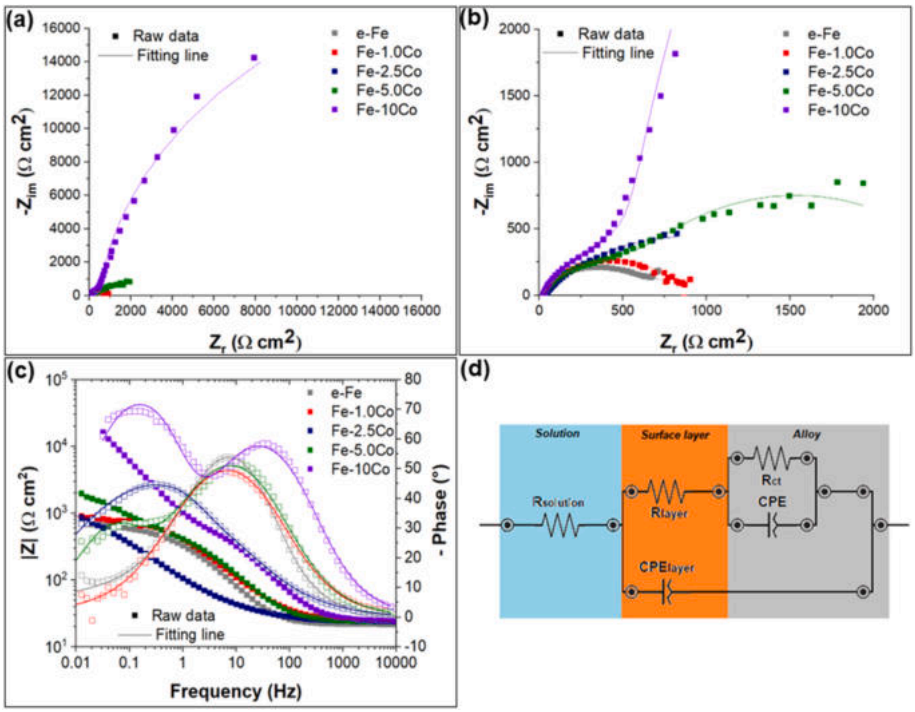

Fig. 7. Representative (a) Nyquist, (b) magnification of Nyquist and (c) Bode plots of the samples. The fitting process was conducted using the equivalent circuit shown in (d).

Table 6
Data obtained from the fitting process.

Sample	R_{sol} (Ω)	R_{layer} (Ω)	R_{ct} (kΩ)	CPE_{layer} x 10^{-4} ($F{\cdot}s^{n-1}$)	n_{layer}	CPE x 10^{-4} ($F{\cdot}s^{n-1}$)	n
e-Fe	22 ± 0.5	34 ± 4	1.05 ± 0.06	8.4 ± 2.7	0.84 ± 0.04	30.0 ± 2.6	0.11 ± 0.01
Fe-1.0Co	24 ± 0.2	147 ± 5	1.22 ± 0.04	3.4 ± 1.6	0.77 ± 0.04	8.1 ± 0.6	0.12 ± 0.01
Fe-2.5Co	24 ± 0.3	238 ± 69	1.52 ± 0.03	2.7 ± 0.8	0.80 ± 0.03	16.0 ± 1.9	0.76 ± 0.33
Fe-5.0Co	24 ± 0.7	711 ± 74	1.94 ± 0.21	3.0 ± 1.2	0.61 ± 0.06	22.9 ± 5.2	0.75 ± 0.09
Fe-10Co	22 ± 2.3	1128 ± 51	42.13 ± 0.82	0.6 ± 0.5	0.76 ± 0.07	2.1 ± 0.9	0.97 ± 0.02

Note: n_{layer} and n are dimensionless parameters.

one single one at middle-low frequency, suggesting the predominat effect of the metal/solution interface, and indicating lower effectiveness of the passive layer in preventing corrosion phenomena. Nevertheless, it could be observed that as the amount of cobalt increased, a higher $|Z|_{max}$ was obtained, indicating a general increase in the corrosion resistance of the alloys. This result was aligned with the increasing E_{corr} value obtained in the polarization test, indicating that the addition of cobalt induced the obtention of alloys more resistant to oxidation.

To investigate the contribution of each feature of the electrolyte-alloy in the corrosion phenomenon, a fitting process was performed; the data is shown in Table 6. From the results of charge transfer resistance (R_{ct}) and resistance of the passive layer (R_{layer}), it was possible to confirm that the addition of cobalt resulted in superior corrosion resistance, as also shown in the polarization test. However, these results seemed controversial when compared to the ones obtained in the polarization test for sample Fe-5.0Co, which showed a superior CR and an inferior R_p than the other alloys. These differences between the two techniques can occur, as they are due to their different nature: in a PDP analysis, the samples are submitted to a high perturbation, whereas for EIS, a steady-state one is performed. The finding that sample Fe-5.0Co presented the highest CR in PDP, but an increasing $|Z|_{max}$ and a R_{ct} few affected might indicate the existence of a layer of low stability at this specific condition, which breaks at strong anodic overpotentials. It is important to note that this condition was the one presenting the most heterogeneous surface among all the conditions.

Nevertheless, a higher value of constant-phase element of the passive layer (CPE_{layer}) was observed in this sample. Increased CPE can be due to penetration of solution into the passive layer, e.g. through existing pores, which increase the permittivity of the capacitor and its capacitance [68,69]. Since the impedance of a capacitor is inversely proportional to its capacitance, increasing the capacity of the passive layer reduces its impedance. The fact that the CPE exponent of the passive layer (n_{layer}) value was also the lowest one also suggested a more pronounced resistor behavior [70], which could indicate presence of solution into the passive layer.

No indications of pitting corrosion were observed in the electrochemical measurements, e.g., inductive loop in the Nyquist plots and/or decrease in |Z| at low frequencies. Most samples, apart from e-Fe and Fe-1.0Co, exhibited predominantly capacitive behavior in the Bode plots, which is not expected for samples undergoing pitting corrosion.

Cytotoxicity was evaluated at one day through Alamar Blue essay and the results are shown in Fig. 8a–c. Three different extracts were evaluated (100 %, 10 % and 1 %). The use of different extracts could better mimic the *in vivo* environment, creating an environment more like the one found in *in vivo* conditions, and eliminating side effects caused by an excessive ions local concentration from the alloy degradation, such as pH changes [71–73].

From the pure extract (Fig. 8a), the e-Fe (**$p < 0.01$), Fe-5.0Co (***$p < 0.001$) and Fe-10Co (*$p < 0.05$) samples were able to significantly decrease the cell viability compared to the CTRL Plast (**$p < 0.01$) condition. For the 10 % diluted extraction (Fig. 8b), both the e-Fe and Fe-1.0Co were able to significantly reduce the viability of the treated

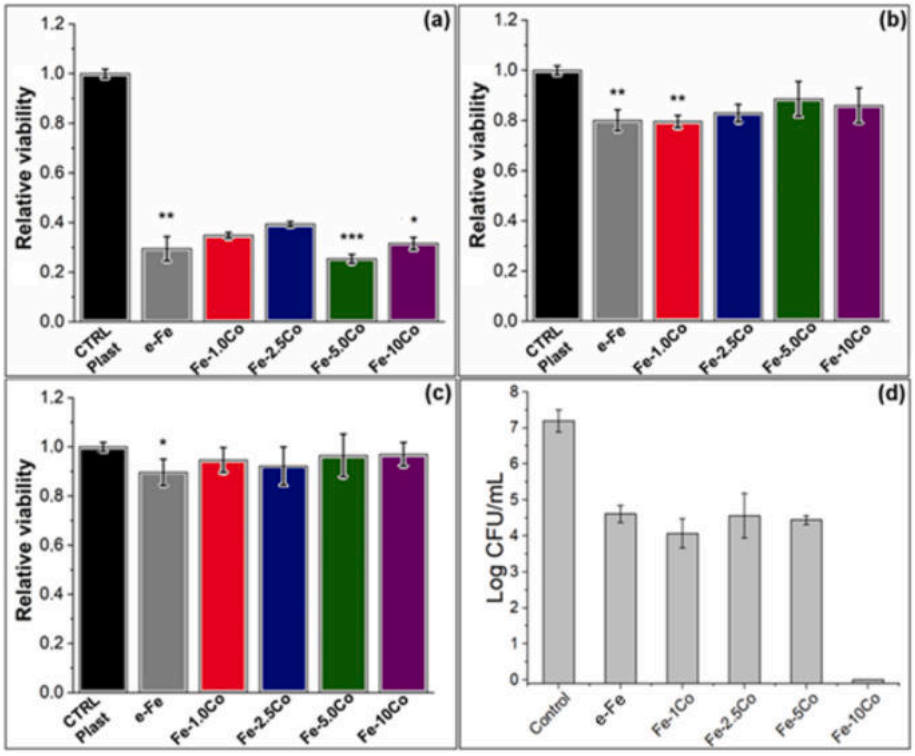

Fig. 8. Cell viability of the samples, measured with extract: (a) 100 % - **p < 0.01 *vs.* CTRL Plast; ***p < 0.001 *vs.* CTRL Plast, *p < 0.05 *vs.* CTRL Plast; (b) 10 % - **p < 0.01 *vs.* CTRL Plast; and (c) 1 % - *p < 0.05 *vs.* CTRL Plast; (d) Comparison of log reduction value of the samples with the control, for the antibacterial test.

HDFs compared to the CTRL Plast condition (**p < 0.01), and no other significant differences were noted among the experimental conditions. Finally, for the 1 % dilution (Fig. 8c), only the e-Fe condition significantly lowered the viability of the treated cells compared to the CTRL Plast condition (*p < 0.05). Once again, no other significant differences were noted in between the tested conditions. From these preliminary cell viability results, it could be observed that electroformed Fe-Co alloys induce a cytotoxic effect towards fibroblasts when used at 100 % concentration. This effect could be caused by the increased and uncontrolled metal ions release [74,75], leading to toxicity towards human cells. However, it must be noted that the model used to perform these tests was characterized by static conditions, which did not represent the highly dynamic conditions found once the material is implanted in the human body. In fact, in the physiological environment, body fluids, such as blood, actively disperse and dilute the degradation products obtained from the material, resulting in lower concentrations. For this reason, tests have also been carried out using diluted extract (10 % and 1 %) to better mimic concentrations that could be found after implantation. As shown in Fig. 8b and c, the fibroblasts viability increased with dilution, resulting being above 70 % for all the tested conditions at both concentrations. This clearly shows that the observed cytotoxicity at 100 % is not due to an inherent toxicity of the extract but rather to their concentration.

To further investigate the response of HDFs cells to the degradation products released by the developed alloys, we utilized ChromaLIVE^{TM}, a mix-and-read Live Cell Painting assay that has been shown to generate a unique phenotypic signature across a wide range of cellular states. This assay enables kinetic tracking of complex cell dynamics, associated with both cell heath and death pathways, thus providing valuable mechanistic insights into treatment-induced phenotypic responses [76]. Representative images of the treated HDFs are shown in Fig. S3 of the Supplementary Materials.

The data analysis of image-based profiles revealed treatment-specific and time-dependent cellular responses across the different treatment conditions. As depicted in the t-SNE plots, at 1 h post-treatment, all the tested conditions, apart from H_2O_2, were grouped within the same cluster, demonstrating no significant morphological changes relative to the CTRL condition (Fig. 9a). This suggested that the exposure time was not sufficient to induce a pronounced alteration in the cell phenotype. At 4 h, the H_2O_2 treatment remained in a separate phenotypic space (Fig. 9b), as evidenced by a unique staining pattern (Fig. S2), highlighting its potency to induce a specific phenotype even with short exposure times. As for the other conditions, despite displaying a broader distribution compared to the 1 h time point, they still clustered together. This suggested a more pronounced phenotypic heterogeneity among the conditions evolving over time, yet not fully distinguishable from the CTRL condition. At 8 h, most treatments, including the experimental conditions, remained grouped with the CTRL condition (Fig. 9c). However, the cluster became more compact, suggesting the emergence of a dominant and potentially convergent phenotype shared across these conditions. In addition, a further increase in the phenotypic distance was observed between this main cluster and the H_2O_2 condition, with the latter forming a well-defined cluster. Interestingly, a new cluster corresponding to staurosporine-treated cells clearly distinct from both the main and the H_2O_2 clusters emerged, which indicated the onset of a phenotypic transition, uniquely driven by staurosporine's mode of action. After 24 h, a more pronounced phenotypic divergence among treatment conditions was observed (Fig. 9d). While erastin, thapsigargin and rapamycin still belonged to the same cluster, likely due to an insufficient exposure time to elicit compound-specific phenotypes, all other conditions were spatially segregated, each forming a distinct phenotypic cluster. Of interest, both experimental conditions, e-Fe and Fe-5.0Co, are clustered together and completely separated from any other conditions, suggesting a shared mechanism of action distinct from the reference compounds.

These findings were consistent with cytotoxicity results showing a significant decrease in cell metabolic activity following 24 h of treatment with high-concentration extracts (Fig. 8). Together, the results not only confirmed the cytotoxic effect of the extracts at high concentration but also suggested that the observed extract-induced cytotoxicity was

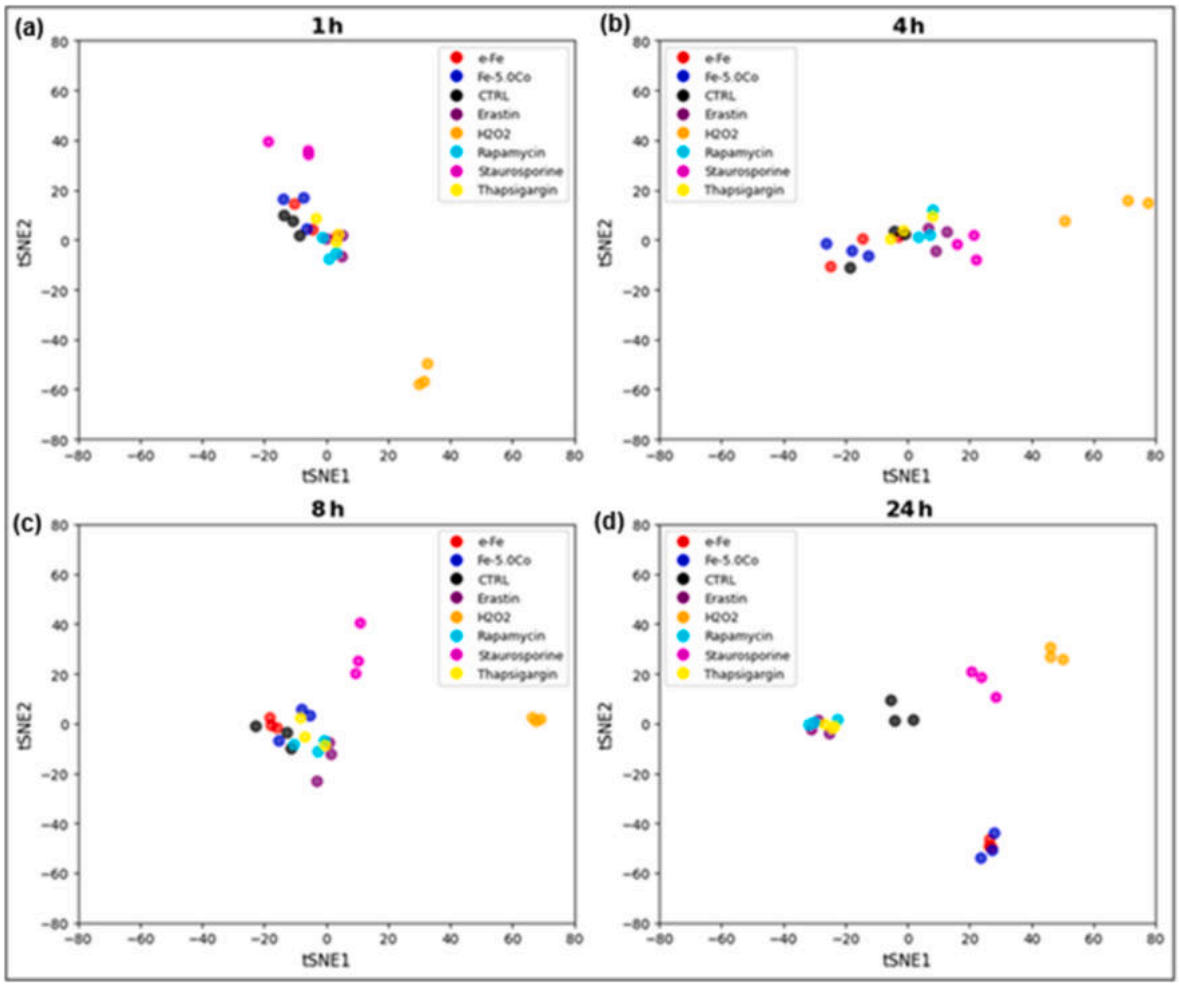

Fig. 9. t-SNE plots illustrating the temporal evolution of HDFs phenotypes: (a) 1 h, (b) 4 h, (c) 8 h and (d) 24 h. Image-based profiles extracted from ChromaLIVE™-stained cells were projected into the t-SNE phenotypic space, with the first two t-SNE components as the axes of the plots. Each color represents a distinct treatment condition, and each dot corresponds to a single replicate. The dynamic shifts in cluster distribution reveal treatment-specific and time-resolved changes in cell phenotype.

Table 7
Summary table of the key findings of the study.

Sample	R_a at 1 × 1 μm^2 (nm)	CR (mm·y^{-1})	R_{ct} (kΩ)	Relative cell viability at 1 % extract (%)	Bacterial reduction (%)
e-Fe	20.6	0.17 ± 0.02	1.05 ± 0.06	0.90 ± 0.05	99.75
Fe-1.0Co	19.0	0.18 ± 0.01	1.22 ± 0.04	0.95 ± 0.05	99.91
Fe-2.5Co	16.2	0.09 ± 0.02	1.52 ± 0.03	0.92 ± 0.08	99.63
Fe-5.0Co	27.6	0.29 ± 0.02	1.94 ± 0.21	0.97 ± 0.09	99.86
Fe-10Co	19.5	0.06 ± 0.02	42.13 ± 0.82	0.97 ± 0.05	100.00

Table 8
Value of CR reported for some biodegradable alloys.

Alloy	CR (mm·y^{-1})	Media	Reference
Pure Fe	0.17	Modified HBBS	This study
Fe-5.0Co	0.29	Modified HBSS	This study
Mg-4Zn-4Ga	~0.20	HBSS	[82]
Zn-5La	0.29	HBSS	[83]
Fe-Mn-5Si	0.25	HBSS	[84]
Zn-0.4Fe	0.50	HBSS	[85]

mediated by different mechanisms than those triggered by the tested reference compound. Both Fe- [77] and Co-ions [78] and compounds were known to induce ferroptosis, a specific type of programmed cell death characterized by the accumulation of lipid peroxides [79]. However, the fact that both experimental compounds appeared in a different cluster reinforces the hypothesis of a particular phenotype. It can be speculated that the use of high concentration extracts (100 %), that were already shown to induce toxic effects in the treated HDFs (Fig. 8), for this test could have resulted in an earlier appearance of a specific phenotype linked to ferroptosis compared to the reference compound erastin. However, further investigations are needed in order to clearly identify the cellular and molecular mechanism involved in the observed phenotypes to effectively link it to ferroptosis or if, actually, another cell death mechanism. This is particularly important in light of the possible use of the proposed alloys for biomedical application, and in particular for the development of medical devices.

In terms of antibacterial activity, the results are shown in Fig. 8d. Supplementary data is presented in Table S2 of the Supplementary Materials. The amount of viable bacteria in the control (bacteria without

material contact) was approximately 10^7 CFU/mL. For most samples, bacterial viability decreased to 10^4 CFU/mL after contact (reduction of more than 99.5 % of the *E. coli*). No bacterial viability was observed for the Fe-10Co condition. Interestingly, this condtion was also the one presenting the lowest corrosion rate among all the samples, around 0.06 $mm.y^{-1}$. This finding indicates that the antibacterial performance of the system was determined not only by the overall corrosion rate, but also by interfacial processes. The observed antibacterial effect could arise from direct bacterial interaction with the alloy surface combined with local release of Co^{2+} ions, even when the bulk degradation was not significant. In fact, one of the proposed mechanism for antibacterial activity in the studied alloys says that the presence of intermetallic phases can destroy the outer bacterial membrane by contact killing, and also prevent bacterial adhesion and inhibit biofilm formation [80].

3.1. Summary

Table 7 summarizes the key results of this study, providing a clear overview of the characteristics of each electroformed sample.

From Table 7, one can observe that low Co additions led to a slight decrease in R_a values (up to sample Fe-2.5Co). For intermediate Co content, the roughness increased (Fe-5.0Co, 27.6 nm), and then dropped again at higher Co concentrations (Fe-10Co). Regarding the CR values, a general trend toward lower values was observed with increasing Co content, except for sample Fe-5.0Co. The CR for this condition was particularly noteworthy, falling within the ideal range for biodegradable implants (0.2–0.5 $mm{\cdot}y^{-1}$) [81]. For comparison, Table 8 shows CR values of different studies reported in the literature for biodegradable alloys. Meanwhile, R_{ct} values remained on the order of 1 kΩ for low and intermediate Co concentrations but significantly increased at higher Co amounts, suggesting the formation of a protective passive layer.

In terms of biological response, all samples exhibited high cell viability (between 90 and 97 %) at a 1 % extract, indicating low cytotoxic effects for fibroblast after 24 h of incubation even for the condition with the highest CR (Fe-5.0Co). Testing lower extract concentrations can better mimic physiological conditions, reducing side effects caused by the accelerated ion release during metal degradation. For the antibacterial activity, all alloys presented at least 99.6 % of bacterial reduction, reaching 100 % reduction for sample Fe-10Co. Based on these preliminary findings, it is suggested that Fe-Co alloys hold promise as potential bioresorbable materials.

4. Conclusion

In this work, electroformed Fe-Co alloys were produced containing different concentrations of cobalt. Results revealed a complex and non-linear relationship between cobalt concentration, microstructural and morphological properties, and degradation behavior. For all the samples, α-Fe phase was observed and the increase in cobalt resulted in alloys with higher crystallinity and rugosity, in addition to an improvement in hydrophobicity of the surfaces. For low and high cobalt additions, the surfaces and topographies appeared homogeneous, whereas an intermediate concentration, as in the Fe-5.0Co sample, produced a more irregular topography, as evidenced by SEM and AFM analyses. This result was probably related to a transition between different nucleation mechanisms, leading to surface with heterogeneous features, high nano-scale roughness and an unstable passive layer. Consequently, the corrosion rate for this condition was almost twice that of pure electroformed Fe. Finally, cell viability tests and the use of AI showed that the alloys presented a unique concentration-dependent cytotoxicity to fibroblasts at one day of incubation. Furthermore, the Fe-Co alloys presented antibacterial activity toward *E. coli*, with a direct kill mechanism. The findings of the study open new directions for exploring electroformed Fe-based alloys. As a first thing, to confirm the increased corrosion rates for the studied condition, complementary techniques such as transmission electron microscopy (TEM) and/or electron backscatter diffraction (EBSD) should be performed. Then, future studies on clarifying the death mechanism of cells, the influence of Co concentration on the nucleation and growth mechanisms, as well as on assessing corrosion properties over longer immersion periods, are encouraged.

Declaration of competing interest

The authors declare that they have no known competing financial interests or personal relationships that could have appeared to influence the work reported in this paper.

Acknowledgements

This project was partially supported by NSERC-Canada, PRIMA-Quebec, and the Quebec University Research Hospital. The authors also would like to thank the PhD student Lidi Astrid Yáñez Hernández (Laval University) for the technical support for the antibacterial test.

Appendix A. Supplementary data

Supplementary data to this article can be found online at https://doi.org/10.1016/j.jmrt.2026.01.020.

Data availability

Data will be made available on request.

References

[1] Bowen PK, Shearier ER, Zhao S, Guillory RJ, Zhao F, Goldman J, Drelich JW. Biodegradable metals for cardiovascular stents: from clinical concerns to recent zn-alloys. Adv Healthcare Mater 2016;5:1121–40. https://doi.org/10.1002/adhm.201501019.
[2] Toong DWY, Ng JCK, Huang Y, Wong PEH, Leo HL, Venkatraman SS, Ang HY. Bioresorbable metals in cardiovascular stents: material insights and progress. Materialia (Oxf) 2020;12:100727. https://doi.org/10.1016/j.mtla.2020.100727.
[3] Khan AR, Grewal NS, Zhou C, Yuan K, Zhang H-J, Jun Z. Recent advances in biodegradable metals for implant applications: exploring in vivo and in vitro responses. Results Eng 2023;20:101526. https://doi.org/10.1016/j.rineng.2023.101526.
[4] Beraldo CHM, Versteg A, Spinelli A, Scharnagl N, da Conceição TF. Anticorrosive properties of chitosan-derivatives coatings on Mg AZ31 alloy in Hank's balanced salt solution. Int J Biol Macromol 2024;260:129390. https://doi.org/10.1016/j.ijbiomac.2024.129390.
[5] Ikeo N, Nakamura R, Naka K, Hashimoto T, Yoshida T, Urade T, Fukushima K, Yabuuchi H, Fukumoto T, Ku Y, Mukai T. Fabrication of a magnesium alloy with excellent ductility for biodegradable clips. Acta Biomater 2016;29:468–76. https://doi.org/10.1016/j.actbio.2015.10.023.
[6] García-Mintegui C, Córdoba LC, Buxadera-Palomero J, Marquina A, Jiménez-Piqué E, Ginebra M-P, Cortina JL, Pegueroles M. Zn-Mg and Zn-Cu alloys for stenting applications: from nanoscale mechanical characterization to in vitro degradation and biocompatibility. Bioact Mater 2021;6:4430–46. https://doi.org/10.1016/j.bioactmat.2021.04.015.
[7] Wątroba M, Bednarczyk W, Kawałko J, Mech K, Marciszko M, Boelter G, Banzhaf M, Bała P. Design of novel Zn-Ag-Zr alloy with enhanced strength as a potential biodegradable implant material. Mater Des 2019;183:108154. https://doi.org/10.1016/j.matdes.2019.108154.
[8] Mouzou E, Paternoster C, Tolouei R, Chevallier P, Biffi CA, Tuissi A, Mantovani D. CO2-rich atmosphere strongly affects the degradation of Fe-21Mn-1C for biodegradable metallic implants. Mater Lett 2016;181:362–6. https://doi.org/10.1016/j.matlet.2016.06.017.
[9] Loffredo S, Paternoster C, Giguère N, Barucca G, Vedani M, Mantovani D. The addition of silver affects the deformation mechanism of a twinning-induced plasticity steel: potential for thinner degradable stents. Acta Biomater 2019;98:103–13. https://doi.org/10.1016/j.actbio.2019.04.030.
[10] Moravej M, Prima F, Fiset M, Mantovani D. Electroformed iron as new biomaterial for degradable stents: development process and structure-properties relationship. Acta Biomater 2010;6:1726–35. https://doi.org/10.1016/j.actbio.2010.01.010.
[11] Gąsior G, Szczepański J, Radtke A. Biodegradable iron-based materials—what was done and what more can be done? Materials 2021;14:3381. https://doi.org/10.3390/ma14123381.
[12] Francis A, Yang Y, Virtanen S, Boccaccini AR. Iron and iron-based alloys for temporary cardiovascular applications. J Mater Sci Mater Med 2015;26:138. https://doi.org/10.1007/s10856-015-5473-8.

[13] Huang T, Zheng Y, Han Y. Accelerating degradation rate of pure iron by zinc ion implantation. Regen Biomater 2016;3:205–15. https://doi.org/10.1093/rb/rbw020.
[14] Huang T, Cheng J, Zheng YF. In vitro degradation and biocompatibility of Fe–Pd and Fe–Pt composites fabricated by spark plasma sintering. Mater Sci Eng C 2014;35:43–53. https://doi.org/10.1016/j.msec.2013.10.023.
[15] Kupková M, Kupka M, Morovská Turoňová A, Oriňaková R. Microstructural, mechanical and corrosion characteristics of degradable PM biomaterials made from copper-coated iron powders. Materials 2022;15:1913. https://doi.org/10.3390/ma15051913.
[16] Eichenbaum G, Wilsey JT, Fessel G, Qiu Q-Q, Perkins L, Hasgall P, Monnot A, More SL, Egnot N, Sague J, Marcello S, Connor K, Scutti J, Christian WV, Coplan PM, Wright J, Hastings B, Katz LB, Vreeke M, Calistri-Yeh M, Faiola B, Purushothaman B, Nevelos J, Bashiri M, Christensen JB, Kovochich M, Unice K. An integrated benefit-risk assessment of cobalt-containing alloys used in medical devices: implications for regulatory requirements in the European Union. Regul Toxicol Pharmacol 2021;125:105004. https://doi.org/10.1016/j.yrtph.2021.105004.
[17] Leyssens L, Vinck B, Van Der Straeten C, Wuyts F, Maes L. Cobalt toxicity in humans—A review of the potential sources and systemic health effects. Toxicology 2017;387:43–56. https://doi.org/10.1016/j.tox.2017.05.015.
[18] Scansetti G, Botta GC, Spinelli P, Reviglione L, Ponzetti C. Absorption and excretion of cobalt in the hard metal industry. Sci Total Environ 1994;150:141–4. https://doi.org/10.1016/0048-9697(94)90141-4.
[19] Research Triangle Park (NC). National toxicology program, report on carcinogens monograph on cobalt and cobalt compounds that release cobalt ions in vivo: RoC monograph 06. Disposition and Toxicokinetics 2016 [Internet], https://www.ncbi.nlm.nih.gov/books/NBK580284/. [Accessed 24 October 2024].
[20] Chang EL, Simmers C, Knight DA. Cobalt complexes as antiviral and antibacterial agents. Pharmaceuticals 2010;3:1711–28. https://doi.org/10.3390/ph3061711.
[21] Abass AA, Abdulridha W a M, Alaarage WK, Abdulrudha NH, Haider J. Evaluating the antibacterial effect of cobalt nanoparticles against multi-drug resistant pathogens. J Med Life 2021;14:823–33. https://doi.org/10.25122/jml-2021-0270.
[22] Kiani MN, Butt MS, Gul IH, Saleem M, Irfan M, Baluch AH, Akram MA, Raza MA. Synthesis and characterization of cobalt-doped ferrites for biomedical applications. ACS Omega 2023;8:3755–61. https://doi.org/10.1021/acsomega.2c05226.
[23] Baino F, Montazerian M, Verné E. Cobalt-doped bioactive glasses for biomedical applications: a review. Materials 2023;16:4994. https://doi.org/10.3390/ma16144994.
[24] Purnama A, Mostavan A, Paternoster C, Mantovani D. Electroforming as a new method for fabricating degradable pure iron stent. In: Niinomi M, Narushima T, Nakai M, editors. Advances in metallic biomaterials. London: Springer; 2015. p. 85–100. https://doi.org/10.1007/978-3-662-46842-5_4.
[25] Sales V, Paternoster C, Mantovani D, Kolliopoulos G. Fe–Mn alloys electroforming process using choline chloride based deep eutectic solvents. In: International conference on raw materials and circular economy. Basel Switzerland: MDPI; 2021. p. 40. https://doi.org/10.3390/materproc2021005040.
[26] Hussain MS. Synthesis of bulk nanostructured materials by high speed turbulent flow—A method of electrodepositing nanocrystalline nickel. In: Hussain CM, editor. Nanomaterials in chromatography. Elsevier; 2018. p. 55–88. https://doi.org/10.1016/B978-0-12-812792-6.00003-0.
[27] Su Y, Champagne S, Trenggono A, Tolouei R, Mantovani D, Hermawan H. Development and characterization of silver containing calcium phosphate coatings on pure iron foam intended for bone scaffold applications. Mater Des 2018;148:124–34. https://doi.org/10.1016/j.matdes.2018.03.061.
[28] Zhang Y, Roux C, Rouchaud A, Meddahi-Pellé A, Gueguen V, Mangeney C, Sun F, Pavon-Djavid G, Luo Y. Recent advances in Fe-based bioresorbable stents: materials design and biosafety. Bioact Mater 2024;31:333–54. https://doi.org/10.1016/j.bioactmat.2023.07.024.
[29] International Organization for Standardization. ISO 10993-5:2009 - biological evaluation of medical devices. Part 5: tests for in vitro cytotoxicity. 2009.
[30] Nakazono-Kusaba A, Takahashi-Yanaga F, Miwa Y, Morimoto S, Furue M, Sasaguri T. PKC412 induces apoptosis through a caspase-dependent mechanism in human keloid-derived fibroblasts. Eur J Pharmacol 2004;497:155–60. https://doi.org/10.1016/j.ejphar.2004.06.050.
[31] Kwon M-Y, Park E, Lee S-J, Chung SW. Heme oxygenase-1 accelerates erastin-induced ferroptotic cell death. Oncotarget 2015;6:24393–403. https://doi.org/10.18632/oncotarget.5162.
[32] Shinji T, Tetsuji T, Hirotoshi M, Eijiro O, Takeshi M, Yasuyoshi O. Hydrogen peroxide-induced apoptosis and necrosis in human lung fibroblasts: protective roles of glutathione. Jpn J Pharmacol 1999;79:33–40. https://doi.org/10.1254/jjp.79.33.
[33] Lindner P, Christensen SB, Nissen P, Møller JV, Engedal N. Cell death induced by the ER stressor thapsigargin involves death receptor 5, a non-autophagic function of MAP1LC3B, and distinct contributions from unfolded protein response components. Cell Commun Signal 2020;18:12. https://doi.org/10.1186/s12964-019-0499-z.
[34] Zheng W, Qian Y, Chen S, Ruan H, Fan C. Rapamycin protects against peritendinous fibrosis through activation of autophagy. Front Pharmacol 2018;9. https://doi.org/10.3389/fphar.2018.00402.
[35] American Society for Testing and Materials. ASTM E2922-23 - guide for the use of standard test methods and practices for evaluating antibacterial activity on textiles. https://doi.org/10.1520/E2922-23; 2023.
[36] Okamoto H. Co-Fe (Cobalt-Iron). J Phase Equilibria Diffus 2008;29:383–4. https://doi.org/10.1007/s11669-008-9345-5.
[37] Shen XP, Harris SJ, Noble B. Influence of small vanadium and cobalt additions on microstructure and properties of ductile iron. Mater Sci Technol 1995;11:893–900. https://doi.org/10.1179/mst.1995.11.9.893.
[38] Ma ZL, Belyakov SA, Gourlay CM. Effects of cobalt on the nucleation and grain refinement of Sn-3Ag-0.5Cu solders. J Alloys Compd 2016;682:326–37. https://doi.org/10.1016/j.jallcom.2016.04.265.
[39] Anjum S, Tufail R, Rashid K, Zia R, Riaz S. Effect of cobalt doping on crystallinity, stability, magnetic and optical properties of magnetic iron oxide nano-particles. J Magn Magn Mater 2017;432:198–207. https://doi.org/10.1016/j.jmmm.2017.02.006.
[40] Nik Rozlin NM, Alfantazi AM. Nanocrystalline cobalt–iron alloy: synthesis and characterization. Mater Sci Eng, A 2012;550:388–94. https://doi.org/10.1016/j.msea.2012.04.092.
[41] Moravej M. Développement et validation des matériaux métalliques pour stents cardiovasculaires biodégradables. PhD Thesis. Laval University; 2011. Www.Theses.Ulaval.Ca/2011/27897/27897.
[42] Mostavan A, Paternoster C, Tolouei R, Ghali E, Dubé D, Mantovani D. Effect of electrolyte composition and deposition current for Fe/Fe-P electroformed bilayers for biodegradable metallic medical applications. Mater Sci Eng C 2017;70:195–206. https://doi.org/10.1016/j.msec.2016.08.026.
[43] Easton MA, Qian MA, StJohn DH. Grain refinement in alloys: novel approaches. In: Reference module in materials science and materials engineering. Elsevier; 2016. https://doi.org/10.1016/B978-0-12-803581-8.03789-9.
[44] Chiu C-W, Sun I-W, Chen P-Y. Electrodeposition and characterization of CoP compounds produced from the hydrophilic room-temperature ionic liquid 1-Butyl-1-Methylpyrrolidinium dicyanamide. J Electrochem Soc 2017;164:H5018–25. https://doi.org/10.1149/2.0041708jes.
[45] Su X, Qiang C. Influence of pH and bath composition on properties of Ni–Fe alloy films synthesized by electrodeposition. Bull Mater Sci 2012;35:183–9. https://doi.org/10.1007/s12034-012-0284-8.
[46] Neuróhr K, Csik A, Vad K, Bartók A, Molnár G, Péter L. Composition depth profile analysis of electrodeposited alloys and metal multilayers: the reverse approach. J Solid State Electrochem 2011;15:2523–44. https://doi.org/10.1007/s10008-011-1465-x.
[47] Wang G, Han J, Lin Y, Zheng W. Investigation on size effect of surface roughness and establishment of prediction model in micro-forming process. Mater Today Commun 2021;27:102279. https://doi.org/10.1016/j.mtcomm.2021.102279.
[48] Rudnik E, Włoch G, Walkowicz M. Effect of electrolysis conditions on electrodeposition of cobalt–tin alloys, their structure, and wettability by liquids. Molecules 2024;29:3084. https://doi.org/10.3390/molecules29133084.
[49] Bazhan Z, Ghodsi FE, Mazloom J. The surface wettability and improved electrochemical performance of nanostructured Co x Fe 3−x O 4 thin film. Surf Coat Technol 2017;309:554–62. https://doi.org/10.1016/j.surfcoat.2016.12.024.
[50] Zangari G. Electrodeposition of alloys and compounds in the era of microelectronics and energy conversion technology. Coatings 2015;5:195–218. https://doi.org/10.3390/coatings5020195.
[51] Landolt D. Electrodeposition science and technology in the last quarter of the twentieth century. J Electrochem Soc 2002;149:S9–20.
[52] Zarebidaki A, Davoodi S. Electrodeposition and characterization of Fe-P coating applied onto mild steel substrate. JOM 2024;76:684–90. https://doi.org/10.1007/s11837-023-06298-0.
[53] Wang W, Wang J, Qi M. Microstructure and in vitro biodegradable properties of Fe-Zn alloys prepared by electroforming. Adv Mater Res 2014;1033–1034:1200–6. https://doi.org/10.4028/www.scientific.net/AMR.1033-1034.1200.
[54] Myung NV, Park DY, Urgiles DE, George T. Electroformed iron and FeCo alloy. Electrochim Acta 2004;49:4397–404. https://doi.org/10.1016/j.electacta.2004.04.031.
[55] Wang X, Xu X, Nie Y, Wang R, Zou J. Electronic-state modulation of metallic co-assisted Co $_7$ Fe $_3$ alloy heterostructure for highly efficient and stable overall water splitting. Adv Sci 2023;10. https://doi.org/10.1002/advs.202301961.
[56] Peuster M, Wohlsein P, Brügmann M, Ehlerding M, Seidler K, Fink C, Brauer H, Fischer A, Hausdorf G. A novel approach to temporary stenting: degradable cardiovascular stents produced from corrodible metal—results 6–18 months after implantation into New Zealand white rabbits. Heart 2001;86:563–9.
[57] Peuster M, Hesse C, Schloo T, Fink C, Beerbaum P, von Schnakenburg C. Long-term biocompatibility of a corrodible peripheral iron stent in the porcine descending aorta. Biomaterials 2006;27:4955–62. https://doi.org/10.1016/j.biomaterials.2006.05.029.
[58] Szymura S, Bala H, Pawłowska G, Rabinovich YuM, Sergeev VV, Pokrovskii DV. Modification of the magnetic properties and corrosion resistance of Nd-Fe-B permanent magnets with addition of cobalt. Journal of the Less Common Metals 1991;175:185–98. https://doi.org/10.1016/0022-5088(91)90003-M.
[59] Kim KH, Lee SH, Nam ND, Kim JG. Effect of cobalt on the corrosion resistance of low alloy steel in sulfuric acid solution. Corros Sci 2011;53:3576–87. https://doi.org/10.1016/j.corsci.2011.07.001.
[60] Evgeny B, Hughes T, Eskin D. Effect of surface roughness on corrosion behaviour of low carbon steel in inhibited 4 M hydrochloric acid under laminar and turbulent flow conditions. Corros Sci 2016;103:196–205. https://doi.org/10.1016/j.corsci.2015.11.019.
[61] Toloei A, Stoilov V, Northwood D. The relationship between surface roughness and corrosion. In: Volume 2B: advanced manufacturing. American Society of Mechanical Engineers; 2013. https://doi.org/10.1115/IMECE2013-65498.
[62] Valadez-Martínez MA, Hernández-Maya LG, Avelino-Jiménez IA, Menchaca-Arredondo J, Garibay-Febles V, Zapata-Peñasco I. Influence of roughness on the early corrosion of API steels by atomic force microscopy (AFM): a real-time

assessment. Mater Today Commun 2023;36:106519. https://doi.org/10.1016/j.mtcomm.2023.106519.
[63] Souza CAC, Ribeiro DV, Kiminami CS. Corrosion resistance of fe-cr-based amorphous alloys: an overview. J Non-Cryst Solids 2016;442:56–66. https://doi.org/10.1016/j.jnoncrysol.2016.04.009.
[64] Berger JE, Jorge AM, Koga GY, Roche V, Kiminami CS, Bolfarini C, Botta WJ. Influence of chromium concentration and partial crystallization on the corrosion resistance of FeCrNiB amorphous alloys. Mater Char 2021;179:111369. https://doi.org/10.1016/j.matchar.2021.111369.
[65] Guo SF, Zhang HJ, Liu Z, Chen W, Xie SF. Corrosion resistances of amorphous and crystalline Zr-based alloys in simulated seawater. Electrochem Commun 2012;24:39–42. https://doi.org/10.1016/j.elecom.2012.08.006.
[66] Cho S, Buchsbaum SF, Biener M, Jones J, Melia MA, Stull JA, Colon-Mercado HR, Dwyer J, Roger Qiu S. True active surface area as a key indicator of corrosion behavior in additively manufactured 316L stainless steel. Mater Des 2024;237:112559. https://doi.org/10.1016/j.matdes.2023.112559.
[67] Sahari A, Azizi A, Schmerber G, Abes M, Bucher JP, Dinia A. Electrochemical nucleation and growth of Co and CoFe alloys on Pt/Si substrates. Catal Today 2006;113:257–62. https://doi.org/10.1016/j.cattod.2005.11.075.
[68] Beraldo CHM, Spinelli A, Scharnagl N, da Conceição TF. Phosphorylated PVA coatings for corrosion protection of Mg AZ31 alloy. J Coating Technol Res 2023;21:243–53. https://doi.org/10.1007/s11998-023-00813-3.
[69] Ribeiro J. Electrochemical impedance spectroscopy: a tool on the electrochemical investigations. Revista Virtual de Química 2020;12:1626–41. https://doi.org/10.21577/1984-6835.20200123.
[70] Jorcin J-B, Orazem ME, Pébère N, Tribollet B. CPE analysis by local electrochemical impedance spectroscopy. Electrochim Acta 2006;51:1473–9. https://doi.org/10.1016/j.electacta.2005.02.128.
[71] Han H-S, Kim H-K, Kim Y-C, Seok H-K, Kim Y-Y. Conventional and improved cytotoxicity test methods of newly developed biodegradable magnesium alloys. Met Mater Int 2015;21:1108–17. https://doi.org/10.1007/s12540-015-5069-3.
[72] Gai X, Liu C, Wang G, Qin Y, Fan C, Liu J, Shi Y. A novel method for evaluating the dynamic biocompatibility of degradable biomaterials based on real-time cell analysis. Regen Biomater 2020;7:321–9. https://doi.org/10.1093/rb/rbaa017.
[73] Wang J, Witte F, Xi T, Zheng Y, Yang K, Yang Y, Zhao D, Meng J, Li Y, Li W, Chan K, Qin L. Recommendation for modifying current cytotoxicity testing standards for biodegradable magnesium-based materials. Acta Biomater 2015;21:237–49. https://doi.org/10.1016/j.actbio.2015.04.011.
[74] Peters K, Staehlke S, Rebl H, Jonitz-Heincke A, Hahn O. Impact of metal ions on cellular functions: a focus on mesenchymal stem/stromal cell differentiation. Int J Mol Sci 2024;25:10127. https://doi.org/10.3390/ijms251810127.
[75] Košir S, Vižintin A, Miklavčič D. Decreases in cell viability resulting from metal ions present in stainless steel in electroporated and nonelectroporated cells. In: International electrotechnical and computer science conference, portorož; 2021. p. 399–402.
[76] Cottet M, Marrero YF, Mathien S, Audette K, Lambert R, Bonneil E, Chng K, Campos A, Andrews DW. Live cell painting: new nontoxic dye to probe cell physiology in high content screening. SLAS Discovery 2024;29:100121. https://doi.org/10.1016/j.slasd.2023.10.005.
[77] Li J, Cao F, Yin H, Huang Z, Lin Z, Mao N, Sun B, Wang G. Ferroptosis: past, present and future. Cell Death Dis 2020;11:88. https://doi.org/10.1038/s41419-020-2298-2.
[78] Montesdeoca N, Johannknecht L, Efanova E, Heinen-Weiler J, Karges J. Ferroptosis inducing Co(III) polypyridine sulfasalazine complex for therapeutically enhanced anticancer therapy. Angew Chem Int Ed 2024;63. https://doi.org/10.1002/anie.202412585.
[79] Dixon SJ, Lemberg KM, Lamprecht MR, Skouta R, Zaitsev EM, Gleason CE, Patel DN, Bauer AJ, Cantley AM, Yang WS, Morrison B, Stockwell BR. Ferroptosis: an iron-dependent form of nonapoptotic cell death. Cell 2012;149:1060–72. https://doi.org/10.1016/j.cell.2012.03.042.
[80] Jiao J, Zhang S, Qu X, Yue B. Recent advances in research on antibacterial metals and alloys as implant materials. Front Cell Infect Microbiol 2021;11. https://doi.org/10.3389/fcimb.2021.693939.
[81] Lelito J, Pierwoła A, Krawiec H, Vignal V, Gondek Ł, Kozieł T, Babilas R, Szucki M, Bała P. Corrosion behavior of Mg72Zn27Pt1 alloy in Hanks' solution: comparison between amorphous and crystalline structures. npj Mater Degrad 2025;9:52. https://doi.org/10.1038/s41529-025-00601-x.
[82] Bazhenov V, Li A, Iliasov A, Bautin V, Plegunova S, Koltygin A, Komissarov A, Abakumov M, Redko N, Shin KS. Corrosion behavior and biocompatibility of hot-extruded Mg–Zn–Ga–(Y) biodegradable alloys. J Funct Biomater 2022;13:294. https://doi.org/10.3390/jfb13040294.
[83] Tong X, Han Y, Zhou R, Zeng J, Wang C, Yuan Y, Zhu L, Huang S, Ma J, Li Y, Wen C, Lin J. Mechanical properties, corrosion and degradation behaviors, and in vitro cytocompatibility of a biodegradable Zn–5La alloy for bone-implant applications. Acta Biomater 2023;169:641–60. https://doi.org/10.1016/j.actbio.2023.07.061.
[84] Rybalchenko O, Anisimova N, Martynenko N, Rybalchenko G, Belyakov A, Shchetinin I, Lukyanova E, Chernogorova O, Raab A, Pashintseva N, Kornyushenkov E, Babayeva G, Sokolova D, Kiselevskiy M, Dobatkin S. Biocompatibility and degradation of Fe-Mn-5Si alloy after equal-channel angular pressing: in vitro and in vivo study. Appl Sci 2023;13:9628. https://doi.org/10.3390/app13179628.
[85] Su Y, Fu J, Lee W, Du S, Qin Y-X, Zheng Y, Wang Y, Zhu D. Improved mechanical, degradation, and biological performances of Zn–Fe alloys as bioresorbable implants. Bioact Mater 2022;17:334–43. https://doi.org/10.1016/j.bioactmat.2021.12.030.